Journal of Fluids and Structures (2000) **14,** 799–817
doi:10.1006/jfls.2000.0300, available online at http://www.idealibrary.com on IDEAL®

MODELING THE UNSTEADY LIFT AND DRAG ON A FINITE-LENGTH CIRCULAR CYLINDER IN CROSS-FLOW

D. E. Capone

Pennsylvania State University, Applied Research Laboratory
P. O. Box 30, State College, PA 16804, U.S.A.

G. C. Lauchle

Pennsylvania State University, Graduate Program in Acoustics and Applied Research Laboratory, P. O. Box 30, State College, PA 16804, U.S.A.

(Received 30 July 1999, and in final form 31 March 2000)

Semi-empirical models for unsteady lift and drag are developed to predict the spectral features of the unsteady forces on a finite-length, right circular cylinder in cross-flow. In general, the models consist of two parts; the spatial variation of r.m.s wall pressure on the cylinder, and the correlation lengths which describe the spatial extent of the correlation of the unsteady wall pressures. Experiments were conducted in a low noise wind tunnel as a function of cylinder diameter Reynolds number ($19\,200 < \mathrm{Re} < 32\,000$) and the Strouhal number ($0{\cdot}05 < \mathrm{St} < 3{\cdot}33$), to measure the statistics of the unsteady wall pressures on a model cylinder. These results are incorporated into the theoretical models, and predictions of the spectral characteristics of the lift and drag are made. The r.m.s. wall pressures on the cylindrical surface are found to have the largest amplitude near the cylinder end-cap, and on the rearward portion of the cylinder body. The high levels in these locations are attributed to the separated flow region over the end-cap. The circumferential and axial length-scales decrease exponentially with Strouhal number. Both length-scales exhibit maxima near the Strouhal shedding frequency of $\mathrm{St} = 0{\cdot}21$. The axial length-scales are found to depend on the measurement reference location due to the three-dimensional flow and separated flow region near the end-cap. The unsteady lift and drag predictions using the models developed in this work agree well with previously measured unsteady force data measured on inertial hydrophones exposed to flow. The broadband unsteady lift is found to be greater than the broadband unsteady drag by nominally 3 dB.

1. INTRODUCTION

Moored or suspended underwater acoustic sensors are used in numerous applications for the measurement and localization of underwater sound sources. The performance of these sensors is degraded by the presence of various background noise sources such as, oceanic ambient noise, electronic noise, mechanical suspension-induced noise, and flow noise. Flow noise results from the sensor being located in an environment where fluid flows over the body of the sensor. In the case of sensors configured as bluff bodies, the fluid is disturbed as it passes over the sensor, resulting in turbulence on the surface and in the wake of the body. The turbulence produces time-dependent pressure fluctuations on the surface of the sensor, which result in unsteady lift and drag forces acting on the sensor. Pressure, pressure gradient, and acoustic velocity hydrophones, in addition to acoustic intensity probes, respond to these unsteady body forces, resulting in a spurious signal known as flow noise.

0889–9746/00/080799 + 19 $35.00/0

The problem is particularly important for inertial sensors; the outputs of which are proportional to velocity or acceleration. One common shape used for underwater acoustic sensors is that of a finite-length right circular cylinder. Finger *et al.* (1979), and McEachern & Lauchle (1995) have shown that the unsteady forces on such finite-length cylinders can result in flow-induced self-noise being the major component of the transducer output signal. Similar results were identified for spherical-shaped hydrophones by Lauchle & Jones (1998).

Significant research has been performed on the measurement and prediction of unsteady lift and drag on two-dimensional, or "infinite length", cylinders in cross-flow. Ribeiro (1992) provided a comprehensive review of the fluctuating lift and spanwise correlation characteristics determined for 2-D cylinders. Considerably less work has been done on finite-length, or 3-D cylinders, due to the complexity of the problem and due to the limited application of the results.

The work of McEachern (1993), and McEachern and Lauchle (1995) quantified the unsteady lift and drag on finite-length, cylindrical-shaped hydrophones of various aspect ratios and end-cap corner radii. They found that the flow-induced noise on a pressure gradient, or acoustic velocity hydrophone decreases as the aspect ratio and corner radii increases. McEachern & Lauchle (1995) observed that the unsteady force spectra are broadband, and contained considerable energy at frequencies above the predicted vortex-shedding frequency. This observation is consistent with those of Keefe (1961) who noted that the flow over the endcap causes a decorrelation of the vortex-shedding process behind the cylinder, resulting in wake energy which is more broadband in nature. Farivar (1981) measured fluctuating pressures and forces on a cylinder with one end free and the other end mounted to the wall of a wind tunnel. The length-to-diameter ratio (L/D) ranges from 2·78 to 12·5 at a Reynolds number based on free-stream velocity and cylinder diameter of $7{\cdot}0 \times 10^4$. Definite vortex-shedding frequencies are present on the signals of the pressure sensors for $L/D > 7{\cdot}5$, but for smaller aspect ratios, no discrete shedding frequency was detected.

Baban *et al.* (1989) measured unsteady forces on both a 2-D cylinder and a 3-D cylinder with one free end. Flow visualization showed an unsteady flow reversal region behind the 3-D cylinder of approximately two cylinder diameters in streamwise length, and of width comparable to the span (L) of the cylinder. A strong correlation between the fluctuating lift and the fluctuating streamwise velocity component was evident for the 2-D case; however, for the 3-D experiment, correlation was essentially nonexistent. The presence of the separated flow over the end of the cylinder inhibits the formation of coherent vortices along the span of the cylinder. Also, the large unsteady recirculation zone behind a finite-length cylinder breaks up the coherent vortices shed by the cylinder. The fluctuating local drag for the 3-D case was found to be larger than the fluctuating local lift measured near the free end of the cylinder.

Due to the complexity of the flow field for any given sensor orientation, no analytical model for the unsteady forces generated on a finite-length circular cylinder in either steady or unsteady flow exists. The objective of this work is to develop semi-empirical models for the statistics of the surface pressure field, in order to predict the spectral features of the unsteady forces on finite-length, right circular cylinders in unifrom, steady cross-flow. These models can be used for the prediction of the statistical features of the flow noise signal of acoustic sensors of interest.

2. THEORY

2.1. General Formulation

The coordinate system for the circular cylinder is shown in Figure 1. The total unsteady drag on a cylinder can be found by the integration of the projected surface pressures in the

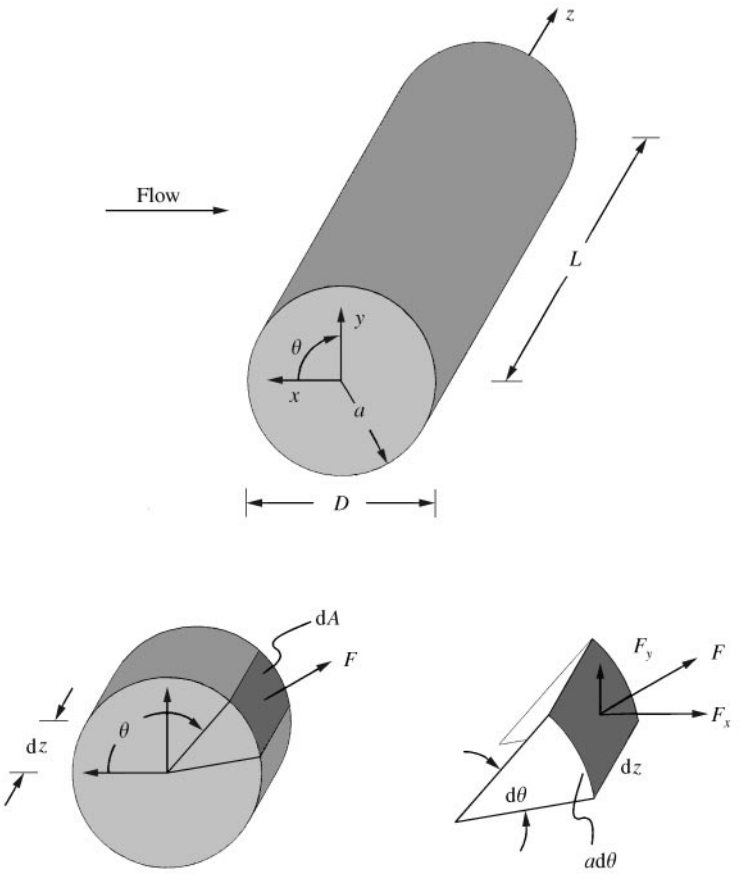

Figure 1. Coordinate system for the right circular cylinder in cross-flow.

x-direction over the surface area of the cylinder:

$$f_x(t) = a \int_0^L \int_0^{2\pi} p(\theta, z, t) \cos\theta \, \mathrm{d}\theta \, dz, \tag{1}$$

where $p(\theta, z, t)$ is the unsteady pressure on the surface of the cylinder body. Similarly, the fluctuating lift can be found by replacing the cosine term in equation (1) with a sine term. The autocorrelation of the unsteady drag, using the notation of Bendat & Piersol (1986) for stationary signals, may be represented as

$$R_{xx}(\tau) = \mathrm{E}[f_x(t) f_x(t + \tau)], \tag{2}$$

where the variable τ is the time displacement between any two signals and E[ ] represents the expected value which is an ensemble average over N records. Substitution of equation (1) into equation (2) yields

$$R_{xx}(\tau) = a^2 \int_0^L \int_0^L \int_0^{2\pi} \int_0^{2\pi} \mathrm{E}[p(\theta, z, t) p(\theta', z', t + \tau)] \cos\theta \, \mathrm{d}\theta \cos\theta' \, \mathrm{d}\theta' \, \mathrm{d}z \, \mathrm{d}z'. \tag{3}$$

Taking the temporal Fourier cosine transform of equation (3) twice, results in the one-sided autospectrum for the unsteady drag:

$$G_{xx}(f) = a^2 \int_0^L \int_0^{2\pi} \int_0^L \int_0^{2\pi} \Gamma(\theta, \theta', z, z', f) \cos\theta \, \mathrm{d}\theta \cos\theta' \, \mathrm{d}\theta' \, \mathrm{d}z \, \mathrm{d}z', \quad f \geqslant 0. \tag{4}$$

Here $\Gamma(\theta, \theta', z, z', f)$ is the one-sided cross-spectral density function of the unsteady pressures on the cylindrical surface. The autospectrum for the unsteady lift is found by replacing the cosine terms in equation (4) with sine terms.

It can be seen by equation (4) that the unsteady lift and drag forces on the cylinder can be calculated if the wall pressure cross-spectra among all points on the body of the cylinder are known. Due to the number of measurements required for this method, few researchers have adopted this approach. However, such measurements are possible, and easier to perform using modern computer-aided data-acquisition methods. In this research we have adopted the approach described in equation (4), and the results are used to form a model of the cross-spectral densities. In the following section, unsteady lift and drag models will be developed in terms of correlation areas so that future calculations of the unsteady forces on similar cylinders in cross-flow can be performed with only a limited number of experimental measurements.

2.2. Models For The Unsteady Lift And Drag

A correlation area, Crighton *et al.* (1992) for unsteady drag is defined as

$$S_{cx}(f, \theta, z) \equiv \frac{a \int_0^L \int_0^{2\pi} \Gamma(f, \theta, \theta', z, z') \cos\theta' \, \mathrm{d}\theta' \, \mathrm{d}z'}{\Gamma(f, \theta, z)}, \tag{5}$$

where $\Gamma(f, \theta, z)$ represents the one-sided autospectrum of the wall pressure fluctuations at locations θ and z. The larger the region over which the pressures are correlated, and hence the larger value for the correlation area, the larger will be the unsteady drag on the cylinder.

If one assumes the circumferential and axial components of the cross-spectral density are separable, similar to the Corcos (1964) theory for turbulent boundary layer wall pressure spectra, the correlation area for unsteady drag can then be represented as

$$S_{cx}(f, \theta, z) \cong a \Lambda_x(f, \theta, z) \Lambda_z(f, \theta, z), \tag{6}$$

where $\Lambda_x(f, \theta, z)$ and $\Lambda_z(f, \theta, z)$ are integral length-scales in the circumferential and axial directions, respectively; see Crighton *et al.* (1992) for a complete description of length-scales. Before defining the integral length-scales for the cylinder, a change of variables will be made in the cross-spectral density representation used in equation (4). In particular, let θ' be replaced by the separation angle $\Delta\theta$, and z' be replaced by the separation distance Δz. The new variables clearly show that the measured cross-spectral densities are a function of both measurement location, and separation distance. With the specified changes in variables, the circumferential correlation length, in radians, for the unsteady drag is defined as

$$\Lambda_x(f, \theta, z) \equiv \int_{-\theta}^{2\pi-\theta} \frac{\Gamma(f, \theta, \Delta\theta)}{\Gamma(f, \theta, z)} \cos(\theta + \Delta\theta) \, \mathrm{d}\Delta\theta, \tag{7}$$

and the circumferential correlation length for the unsteady lift is

$$\Lambda_y(f, \theta, z) \equiv \int_{-\theta}^{2\pi-\theta} \frac{\Gamma(f, \theta, \Delta\theta)}{\Gamma(f, \theta, z)} \sin(\theta + \Delta\theta) \, \mathrm{d}\Delta\theta, \tag{8}$$

The axial correlation length, in the units of z, is defined as

$$\Lambda_z(f, \theta, z) \equiv \int_{-z}^{L-z} \frac{\Gamma(f, z, \Delta z)}{\Gamma(f, \theta, z)} \mathrm{d}\Delta z. \tag{9}$$

The last step in the modeling of the unsteady lift and drag forces, is the definition of a simplified representation for the unsteady surface pressures on the cylinder. Let $\Gamma(f, \theta, z)$ be represented by

$$\Gamma(f, \theta, z) = G_{p,p_r}(f, \theta_r, z_r) A(\theta, z), \tag{10}$$

where $G_{p,p_r}(f, \theta_r, z_r)$ is a reference autospectral density of the wall pressure, p_r, at a specified reference location (θ_r, z_r), and $A(\theta, z)$ is a deterministic function describing the dependence of the mean-square value of the unsteady pressure on measurement location. For this investigation, G_{p,p_r} is taken at the point, $\theta_r = 80^\circ$ and $z_r/D = 1{\cdot}0$. This chosen value of θ_r coincides with the typical position of boundary layer separation from the surface of a cylinder in the subcritical flow regime.

Substitution of equations (10), (9) and (7) into equation (4) results in the final form of the model for the unsteady drag on the cylinder in cross-flow:

$$G_{xx}(f) = G_{p,p_r}(f, \theta_r, z_r) \left\{ a^2 \int_0^L \int_0^{2\pi} \Lambda_x(f, \theta, z) \Lambda_z(f, \theta, z) A(\theta, z) \cos\theta \, \mathrm{d}\theta \, \mathrm{d}z \right\}. \tag{11}$$

Replacing the cosine term in equation (12) with a sine term, and changing to the circumferential lift correlation length, yields the final form of the model for unsteady lift:

$$G_{yy}(f) = G_{p,p_r}(f, \theta_r, z_r) \left\{ a^2 \int_0^L \int_0^{2\pi} \Lambda_y(f, \theta, z) \Lambda_z(f, \theta, z) A(\theta, z) \sin\theta \, \mathrm{d}\theta \, \mathrm{d}z \right\}. \tag{12}$$

The next section will present the experimental methods used to measure the unsteady pressures on the cylinder body. The experiments involve the measurement of the space–frequency correlations of the fluctuating wall pressures. Analysis of the measurements will determine the length-scales and functional forms of the parameters needed in equations (11) and (12).

3. EXPERIMENTAL SETUP

3.1. Wind Tunnel

Fluctuating wall pressure measurements were made on a 0·305 m long and 0·153 m diameter aluminum cylinder in a specially designed low-noise wind tunnel located in a hemi-anechoic chamber. The cylinder was rigidly mounted to a stinger attached to the midpoint of the cylinder at the rearward stagnation point. This mounting arrangement provided a finite-length cylinder with two ends which were free of mounting induced flow disturbances. A side-view of the wind tunnel test-section is shown in Figure 2. The contraction section of the wind tunnel, which has an 11 : 1 contraction ratio, leads to a 0·457 m square test-section, which is 1·50 m long. Downstream, the test-section diffuses at a 7° angle to slow the flow, thereby minimizing acoustic radiation from the trailing edge of the open-ended exit. The cylinder was held by a 0·305 m long sting attached to a vertical steel tube with an aerodynamic cross-section.

Prior to making unsteady pressure measurements on the cylinder, both the mean, U_∞, and the fluctuating, u', velocity field in the test section were characterized. Mean velocity profile surveys were conducted over a plane normal to the flow direction and situated at the leading edge of the cylinder. The flow speeds considered were 1·83, 2·44 and 3·06 m/s, which

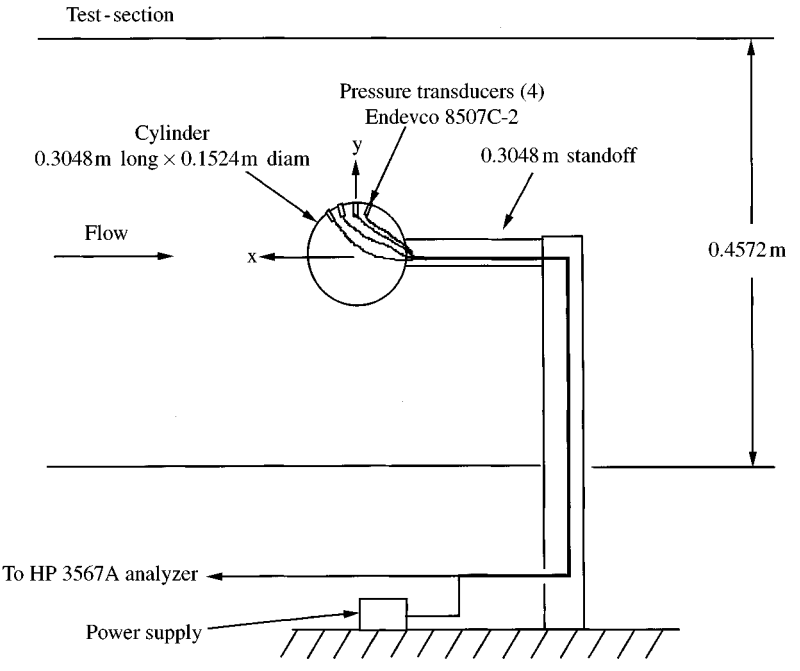

Figure 2. Side view of wind tunnel test-section with cylinder mounted in test position.

correspond to cylinder diameter Reynolds numbers of 19200, 25600, and 32000, respectively. The mean velocity across the test-section was within $\pm$ 2·0% of that measured at the centerline. The streamwise component of turbulence intensity at the same location was less than 0·5% for all three speeds.

3.2. Unsteady Wall Pressure Measurements

Unsteady wall pressure measurements were made at the Reynolds numbers noted in Section 3.1 and over a frequency range of 1–40 Hz, corresponding to Strouhal numbers, fD/U_∞, ranging from 0·05 to 3·33. For brevity, detailed results for Re = 19 200 and 32 000 will be presented in this paper. Results for Re = 25 600 will be used to formulate conclusions and to verify the scaling relationships developed. For all Reynolds numbers, a detailed map of the unsteady wall pressure field on the body of the cylinder was acquired. Spectral data were obtained using a Hewlett Packard (HP) 3567A dynamic signal analyzer. The analyzer was set up with: 256 averages, Hanning window, 800 lines of resolution, and a 2048 line FFT. The acquired data were corrected to a 1 Hz bandwidth. The wind tunnel background noise measurements were made using a 0·635 cm diameter Brüel and Kjær (B&K) model 4138 microphone, and a B&K model 2633 preamplifier. Prior to mounting the model in the test section, the background noise of the tunnel was measured at all three flow speeds using the B&K microphone mounted in a slit tube. The slit tube allows measurement of the background acoustic noise in a wind stream while discriminating against boundary layer flow noise on the sensor. The unsteady pressures on the surface of the cylinder were measured using four individual Endevco 8507C-2 piezoresistive pressure transducers. These transducers have an active sensing diameter of 0·234 cm.

The cylinder model had a series of 2·67 mm diameter holes drilled in the surface, and the transducers were press-fit into these holes. When the holes were not being used for pressure

measurements, they were filled with modeling clay and faired smooth with the surface of the cylinder. Holes were drilled from $\theta = 80$ to 180°, in 10° increments at eight spanwise locations: $z/D = 0{\cdot}08$, 0·17, 0·33, 0·50, 0·67, 0·83, 1·0, and 1·91 measured from the end-cap (Figure 1). At the cylinder centerline, $z/D = 1{\cdot}0$, holes were also drilled from $\theta = 0$ to 80°, in 10° increments. Lastly, at 80 and 90°, a spanwise array of holes were drilled at $z/D = 1{\cdot}33$, 1·50, 1·67, 1·75, and 1·83. The hole locations allowed the pressure transducer measurement locations to be systematically varied over the cylinder in both the circumferential and axial directions.

4. RESULTS

4.1. Unsteady Wall Pressure Power Spectral Densities

The flow field about the cylinder in the θ-direction is expected to be non homogeneous due to laminar, turbulent, and separated flow regions. Figure 3 shows the circumferential variation of the unsteady wall pressure power spectral densities at axial locations $z/D = 1{\cdot}0$ and 0·08. It is evident from Figure 3 that the unsteady wall pressure magnitudes depend on the circumferential measurement location. Although the spectra of the unsteady pressure fluctuations vary with location, the character, or shape, of each curve is consistently the same. The lowest levels are where the boundary layer is laminar and attached to the

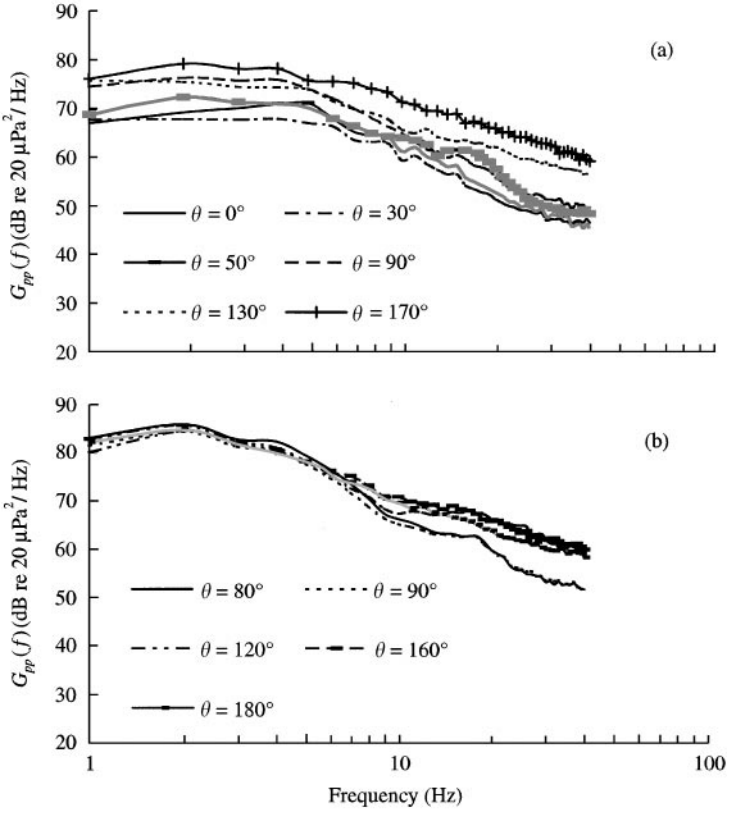

Figure 3. Circumferential variation of the unsteady wall pressure power spectral density for Re = 32 000. (a) $z/D = 1{\cdot}0$, (b) $z/D = 0{\cdot}08$.

surface of the cylinder. They increase towards the rearward portion of the cylinder. Also, as one proceeds from the centerline towards the end-cap of the cylinder ($z/D = 1{\cdot}0$–$0{\cdot}08$) the spectral level increases for a given circumferential location. This result is consistent with the findings of Farivar (1981), who found a maximum in the unsteady wall pressures near the free end of a cantilevered cylinder.

In order to facilitate the modeling of the unsteady forces on the body, a functional form of the root-mean-square (r.m.s.) value of the unsteady wall pressures on the cylinder body was determined using curve-fitting routines. The r.m.s. unsteady wall pressure levels, for Re = 32000 and 19200, are shown in Figure 4. Note that the r.m.s. pressures are normalized by the dynamic head of the free stream, $q = 1/2\rho U_\infty^2$. For Re = 19200, an increase in the unsteady pressure level is evident only for spanwise locations $z/D \leqslant 0{\cdot}33$, while for the higher Re, the level appears to increase continuously with increases in z/D. The general increase in level as the end-cap is approached is not unexpected because a complicated separated flow field exists there, e.g., see flow visualization photographs in McEachern & Lauchle (1995) or McEachern (1993). In general, the boundary layer separates off the leading edge of the end-cap and eventually mixes with the other separated boundary layer that exists on the cylindrical part of the body. At higher values of the Reynolds number, this mixing occurs downstream, away from the measurement transducers; thus, the levels of Figure 4(a) tend to reach their maximum and stay there. At the lower Reynolds number,

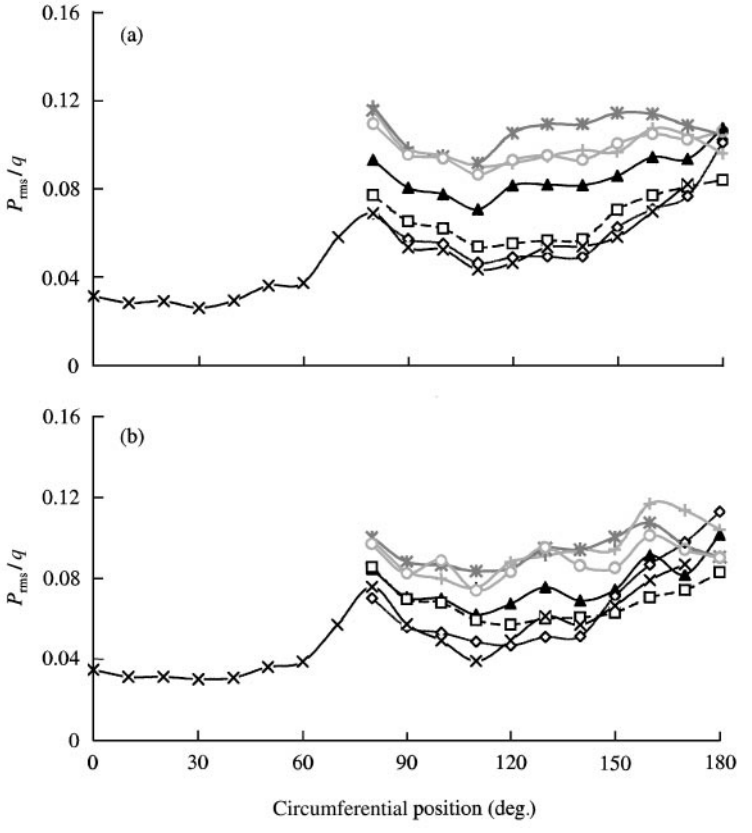

Figure 4. The r.m.s. values of the unsteady wall pressure for all measurement locations on the cylinder body for (a) Re = 32000 (b) Re = 19200: —*—, $z/D = 0{\cdot}08$; —+—, $z/D = 0{\cdot}17$; —○—, $z/D = 0{\cdot}33$; —▲—, $z/D = 0{\cdot}50$; —□—, $z/D = 0{\cdot}67$; —◇—, $z/D = 0{\cdot}83$; —×—, $z/D = 1{\cdot}00$.

Figure 4(b), the mixing zone of these two separated boundary layers moves further upstream and the pressure transducers respond to the increased turbulent activity. Local reattachment of the shear layer also contributes to the high unsteady pressure levels.

The cylinder centerline separation point ($\theta_r = 80^\circ$, $z_r/D = 1{\cdot}0$) is used as the reference location for the autospectral density, $G_{p_r p_r}(f, \theta_r, z_r)$, in equation (10). The reference autospectral density captures the frequency dependence of the unsteady pressures at a well-defined point on the surface of the body. The curve fitting allows us to derive an empirical equation, $A(\theta, z\ D)$, which describes the variation of the r.m.s wall pressures at any location on the cylinder body relative to that at the reference location.

The r.m.s. unsteady wall pressures were modeled in three ways: a third-order polynomial surface fit, a second-order polynomial surface fit, and a separable model. It was found that the separable model of the unsteady wall pressures overpredicted the measured unsteady force on the cylinder by 10 dB. Clearly, the assumption of separability of the circumferential and axial dependence of the unsteady wall pressures is a weak one. Both the second- and third-order polynomial surface fits result in similar predictions of the unsteady forces on the cylinder; however the second-order polynomial surface fit requires four fewer empirical coefficients, six versus 10 . Therefore, results for the second-order polynomial surface fits are presented here. Figure 5 shows a surface plot of the experimental data, and the second-order polynomial surface fit of these data at Re = 32 000. The second-order surface fit is described by

$$A(\theta, z/D) = \frac{p^r_{\text{rms}}}{q}(c_1 z_D^2 + c_2\theta^2 + c_3 z_D\theta + c_4 z_D + c_5\theta + c_6),$$

where

$$c_1 = 0{\cdot}013, \quad c_2 = 0{\cdot}027, \quad c_3 = 0{\cdot}018, \quad c_4 = -0{\cdot}102,$$
$$c_5 = -0{\cdot}125, \quad c_6 = 0{\cdot}242, \quad \text{and } z_D \equiv z/D. \tag{13}$$

The quantity p^r_{rms} is the reference r.m.s. pressure fluctuation value, and the empirical constants c_1–c_6 are an arithmetic average of the coefficients fit for the data from all three Reynolds numbers tested. The second-order polynomial surface fit captures the gross features of the r.m.s values of the wall pressure fluctuations on the body of the cylinder within the range of Reynolds numbers considered. The fine-scale details are not captured because of the models selected.

4.2. Circumferential Cross-Spectral Results

The circumferential length-scales, equations (7) and (8), are calculated using the measured unsteady pressure cross-spectral data as a function of reference location, axial location, and frequency (or Strouhal number). Cross-spectra were measured at discrete pairs of separation points, but the correlation length calculation requires a continuous representation of the cross-spectra as a function of separation distance. Therefore, a third-order polynomial fit to the measured cross-spectral data is numerically integrated to produce the correlation lengths. This process is repeated for each frequency and given reference location. Significant frequency-to-frequency variation was observed in the calculated correlation lengths. This is due to the finite spatial resolution and narrow frequency resolution of the measurements. A finer spatial resolution would provide correlation lengths which are less sensitive to individual cross-spectral results in the curve fitting procedure.

A least-squares fit to the circumferential lengthscales for unsteady lift and drag at five axial locations and Re = 32000 are shown in Figure 6. Additional axial locations and greater detail is shown in Capone (1999). In general, the unsteady drag correlation lengths are shorter than those for the unsteady lift. The correlation lengths all tend to peak around

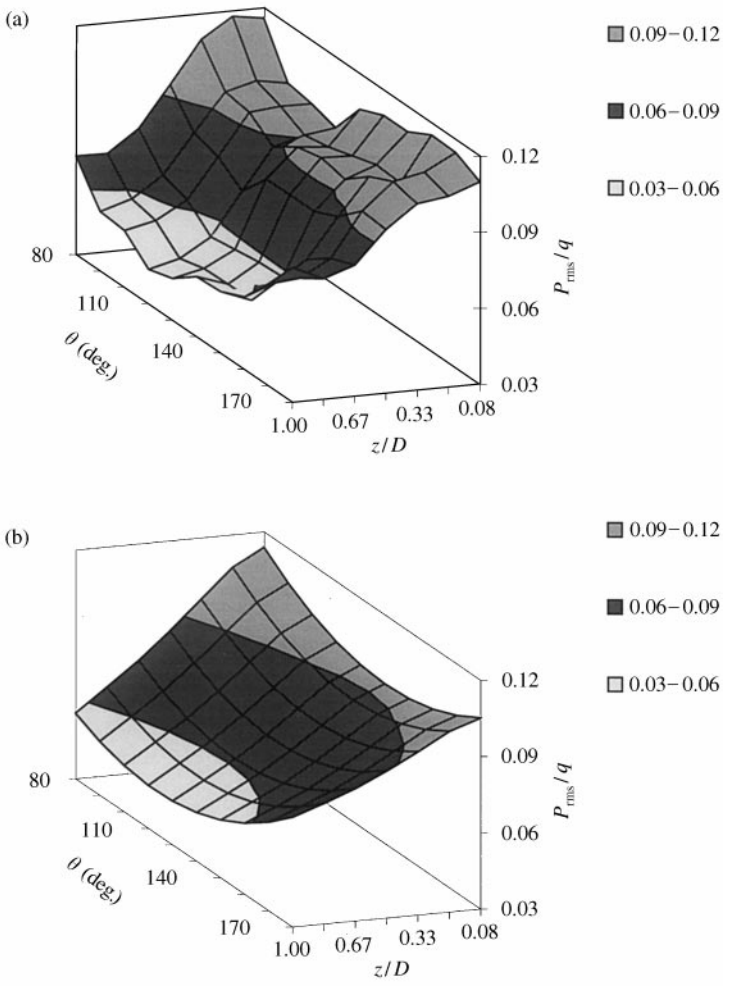

Figure 5. Surface plot and surface fit of the r.m.s. unsteady wall pressures using a second-order polynomial surface fit at Re = 32 000: (a) surface plot; (b) surface fit.

the Strouhal shedding frequency of 0·21. Below St = 0·21 the correlation lengths are small, while above St = 0·21, the lengthscales decrease mildly with increasing St. The boundary layer thickness affects the wake thickness, and essentially the upper limit of the eddy size that can exist within the flow. Below a certain cut-off frequency, in this case around St = 0·21, the flow cannot support structures larger than the largest eddies in the wake; hence, the correlation lengths approach zero very rapidly. Turbulent eddies decorrelate as they convect. The smaller scale, higher frequency eddies decorrelate more rapidly than the larger ones for a given separation distance, resulting in a progressively decreasing correlation length with increasing St.

The Strouhal number dependence of the correlation lengths is modeled using an equation similar to a Rayleigh probability distribution function. Here, the unsteady lift correlation lengths are represented by

$$\Lambda_y(\mathrm{St}) = 1 + \frac{E_1 \mathrm{St}}{E_2^2} \exp\left[\frac{-\mathrm{St}}{(2E_2^2)}\right], \tag{14}$$

where E_1 and E_2 are empirical constants.

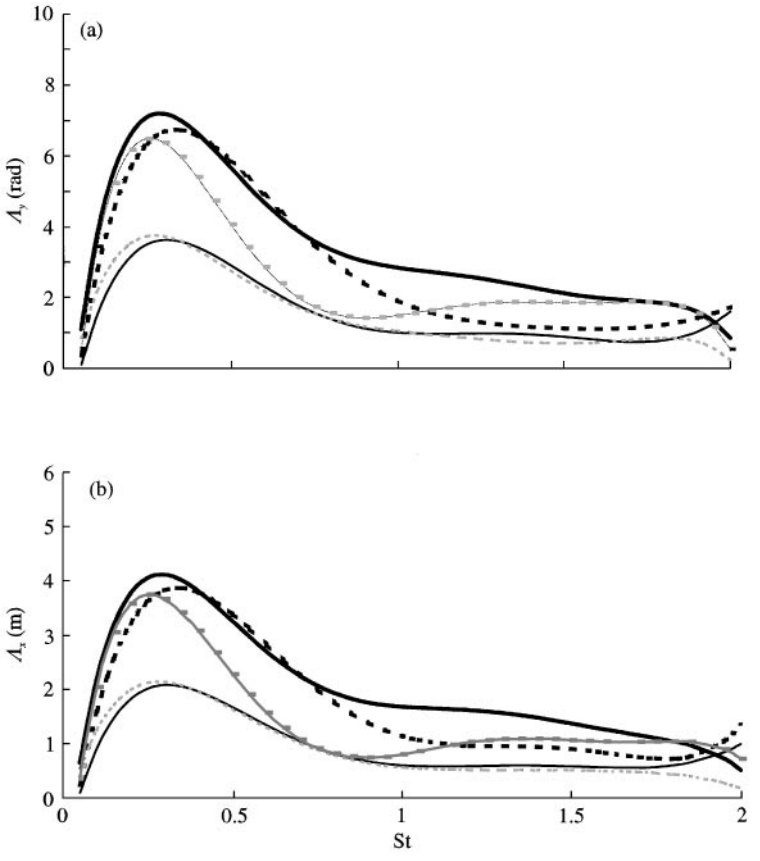

Figure 6. Circumferential correlation lengths for unsteady lift and drag at Re = 32 000 with a reference location of $\theta = 80^\circ$ for (a) unsteady lift, (b) unsteady drag: ——, $z/D = 0{\cdot}08$; - - - - -, $z/D = 0{\cdot}33$; — —, $z/D = 0{\cdot}50$; ——, $z/D = 0{\cdot}83$; - - -, $z/D = 1{\cdot}0$.

The variation of the streamwise correlation lengths with axial location are determined from cross-plots of the length-scale data as a function of z/D. Unfortunately, the data points, as shown in Figure 6, show variation from location to location for certain discrete values of the Strouhal number. Approximately, however, the correlation lengths can be modeled assuming they remain essentially independent of z/D for axial locations, $0{\cdot}5 \leqslant z/D \leqslant 1{\cdot}0$. For axial locations of $z/D < 0{\cdot}5$, the correlation lengths decrease markedly and are more sensitive to changes in z/D. With these assumptions, the empirical curve fit for the axial variation of the unsteady lift length-scales is given by

$$\Lambda_y(z/D) = \exp\left[-\left(\frac{L}{2D} - z/D\right)^2\right], \quad 0{\cdot}0 \leqslant z/D < \leqslant 2{\cdot}0. \tag{15}$$

The final step in modeling the correlation lengths for unsteady lift and drag is to account for the variation in length-scale as a function of reference measurement location. This dependence is examined for circumferential reference locations: $\theta_r = 80^\circ$, 100°, 120°, and 140° and axial locations $z/D = 1{\cdot}00$, $0{\cdot}50$, and $0{\cdot}08$. Figure 7 shows the least-squares fit to the unsteady lift correlation lengths at Re = 32 000 for axial locations of $z/D = 0{\cdot}5$ and $0{\cdot}08$ and for the four circumferential reference locations. It is observed that, for $z/D = 0{\cdot}5$, the

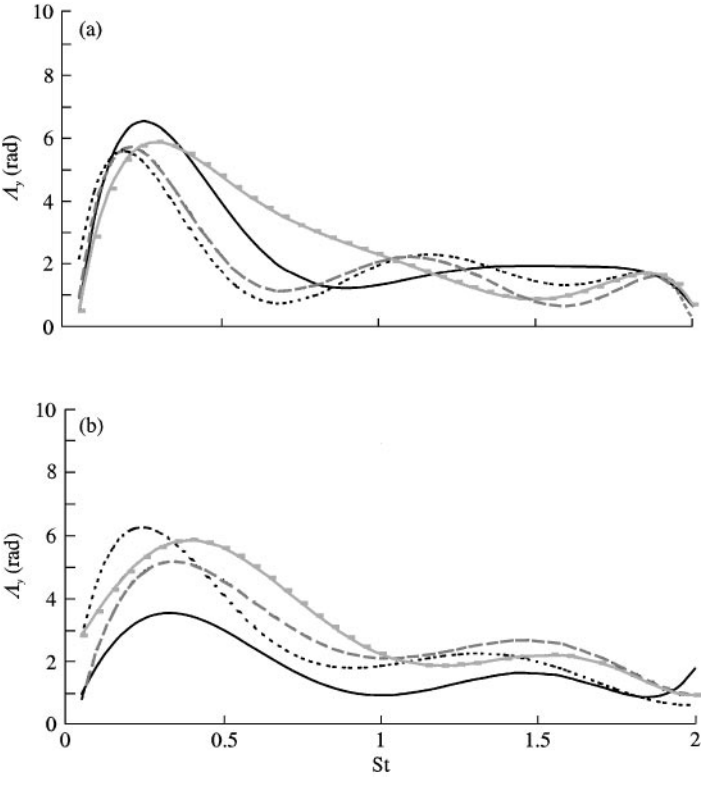

Figure 7. Circumferential correlation lengths for Re = 32 000 and for circumferential reference locations $\theta_r = 80$, 100, 120, and 140° for (a) $z_r/D = 0{\cdot}5$ and (b) $z_r/D = 0{\cdot}8$: ——, $\theta = 80°$; – – –, $\theta = 100°$; - - - - -, $\theta = 120°$; —— —, $\theta = 140°$.

correlation lengths are essentially the same, independent of the reference location. At $z/D = 0{\cdot}08$, a more noticeable variation in the correlation lengths is evident with circumferential reference location $\theta_r = 80°$, especially for Strouhal numbers less than 1·0.

Gershfeld (1996) measured pressure cross-spectra in a spatially inhomogeneous turbulent wall pressure field near a blunt trailing edge of a lifting surface. He concluded, as we have, that the inhomogeneous nature of the wall pressure field can be captured primarily by the streamwise variation in the point power spectra. Here, the inhomogeneity seems to be most pronounced as the end-cap is approached. Sectional unsteady lift coefficients measured by Baban, *et al.* & Ottugen (1989) for a cantilevered cylinder, also show a slight decrease as one progresses towards the free end. Baban *et al.* attributed this to the highly three-dimensional flow near the end-cap which obviously contributes to the spanwise inhomogeneity observed for $z/D = 0{\cdot}08$. Because the increase in lift correlation length is primarily evident only in the $z/D = 0{\cdot}08$ axial range and for $\mathrm{St} < 1{\cdot}0$, the final form of the model for the circumferential length-scales will assume reference location independence.

Based upon the assumptions discussed above, the final form for the circumferential length-scales for unsteady lift and drag are obtained from equations (14) and (15):

$$\Lambda_y(\mathrm{St}, z/D) = \left(1 + \frac{E_1 \mathrm{St}}{E_2^2} \exp\left[\frac{-\mathrm{St}}{(2E_2^2)}\right]\right) \exp\left[-\left(\frac{L}{2D} - z/D\right)^2\right], \tag{16a}$$

$$\Lambda_x(\mathrm{St}, z/D) = \left(1 + \frac{E_3 \mathrm{St}}{E_2^2} \exp\left[\frac{-\mathrm{St}}{(2E_4^2)}\right]\right) \exp\left[-\left(\frac{L}{2D} - z/D\right)^2\right], \tag{16b}$$

where

$$E_1 = 5{\cdot}0, \quad E_2 = 0{\cdot}39 \quad \text{and } E_3 = 5{\cdot}0.$$

Predictions using equation (16) are compared to the circumferential length-scales at Re = 32000 in Figure 8.

4.3. Axial Cross-Spectral Results

The axial length-scales, equation (9), were also calculated from the measured unsteady pressure cross-spectral data. These length-scales are computed as a function of reference location, streamwise location, and frequency, and a suggested model form is derived.

The least-squares fit to the axial length-scales at Re = 32 000 and 19 200 for circumferential locations of $\theta = 80$, 120, 140, and 180°, and a reference location of $z_r/D = 0{\cdot}08$ are shown in Figure 9. As with the circumferential length-scales, the higher frequency, smaller scale eddies which produce the high-frequency pressure fluctuations decay faster than the lower frequency eddies, which results in a general decrease in Λ_z with increasing frequency.

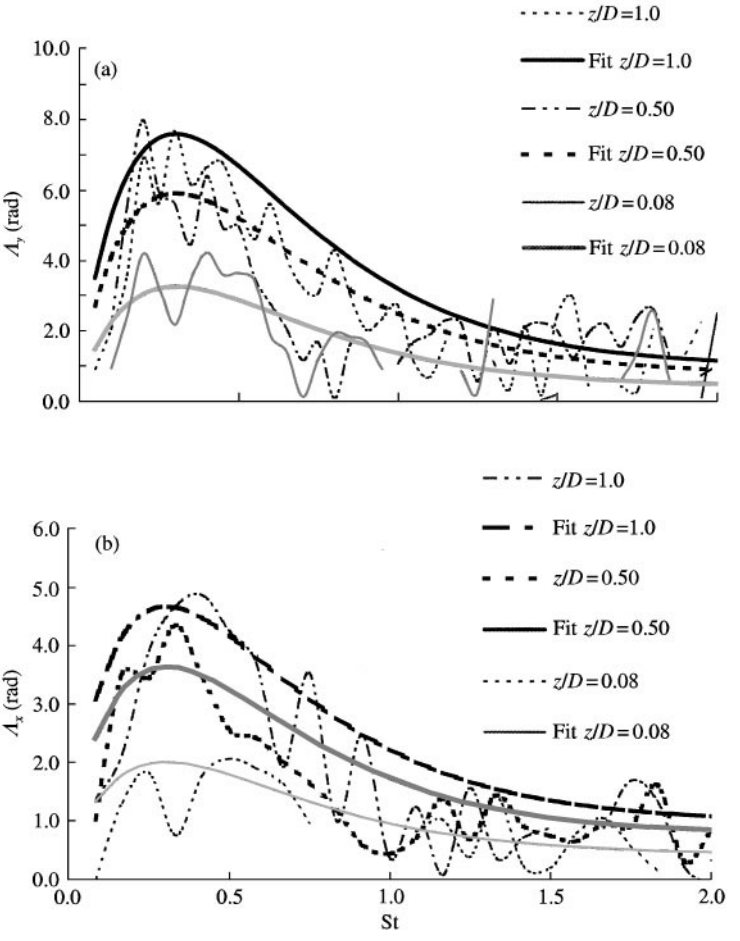

Figure 8. Empirical fit of the correlation lengths for unsteady lift and drag as a function of Strouhal number and axial location compared to measured data with a reference location of $\theta = 80°$ and Re = 32 000 (a) unsteady lift, (b) unsteady drag.

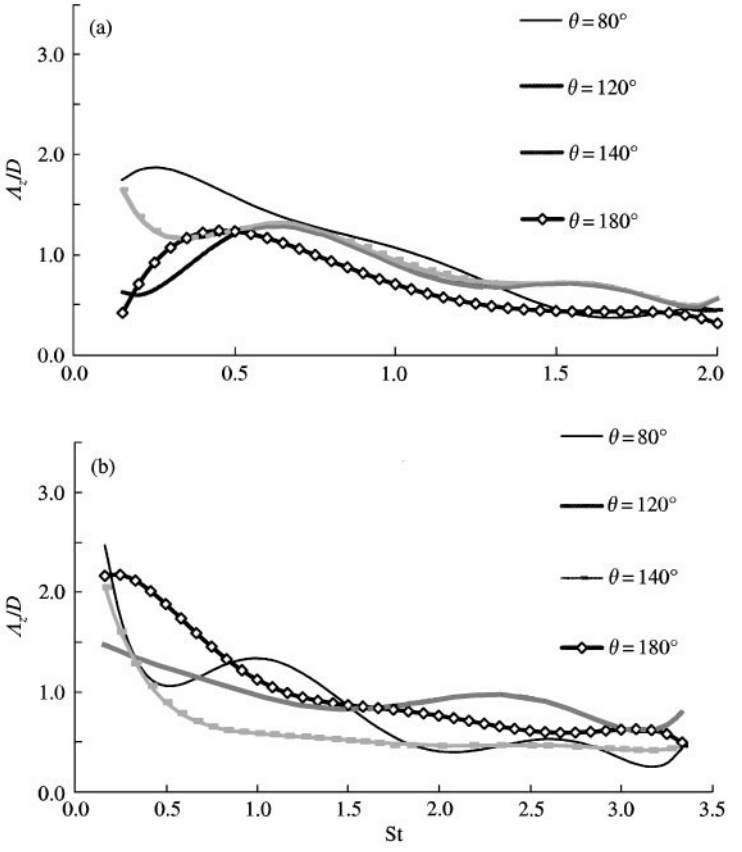

Figure 9. Axial length-scales at Re = 32 000 and 19 200 for circumferential locations of $\theta = 80$, 100, 120, 140, and 180°, and a reference location of $z/D = 0{\cdot}08$ for (a) Re = 32 000, (b) Re = 19 200.

The axial length-scales measured for all three Reynolds numbers are very similar in magnitude and spectral shape, consistent with West & Apelt (1997) who found that the spanwise length-scales on infinite cylinders are independent of Reynolds number over the range 10^4–$2{\cdot}1 \times 10^5$. We will further assume that the dependence of Λ_z on θ is negligible. The Strouhal number dependence of the axial correlation lengths is therefore modeled using the empirical fit of the form

$$\frac{\Lambda_z}{D}(\mathrm{St}) = E_4 \exp[-\mathrm{St}^{0{\cdot}75}]. \tag{17}$$

The dependence of the axial length-scales on axial reference location is established by examining the data from only two circumferential locations because of the assumption that they are independent of circumferential location at constant z/D. Figure 10 shows the least-squares fit to the spanwise correlation lengths for $\theta_r = 100$ and 140° at Re = 32 000. The correlation lengths increase as the reference location is moved towards the center of the cylinder. This behavior is due to the fact that the flow near the center of the cylinder is less disturbed by 3-D end-cap-flow effects. The flow is more two-dimensional, and a larger axial correlation length is expected.

The variation of the axial correlation length with axial reference location is determined from cross-plots of the data of Figure 10. Similar to the circumferential length-scales, the

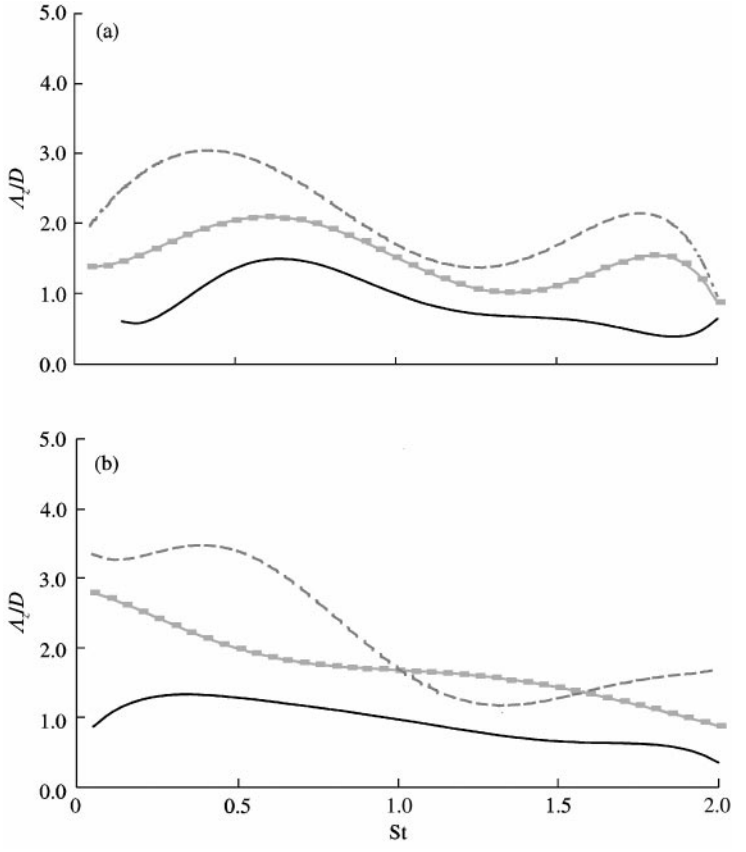

Figure 10. Axial correlation lengths for Re = 32 000 and for reference locations of $z/D = 0{\cdot}08$, $0{\cdot}50$, and $1{\cdot}0$ and (a) $\theta_r = 100^\circ$, (b) $\theta_r = 140^\circ$: ——, $z/D = 0.08$; — — —, $z/D = 0{\cdot}5$; – – –, $z/D = 1{\cdot}0$.

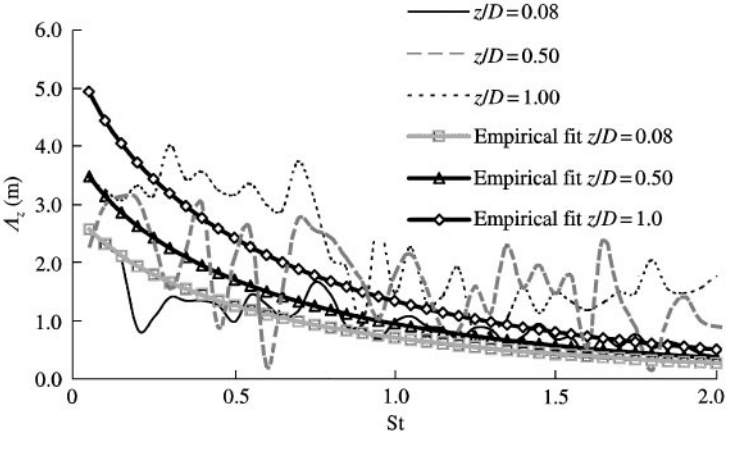

Figure 11. Empirical fit of axial length-scales for various axial locations as a function of Strouhal number for $\theta_r = 140^\circ$ and Re = 32 000.

axial length-scales show an approximately exponential decrease with decreasing z/D. Combining equation (17) with this exponential function, yields

$$\frac{\Lambda_z}{D}(\mathrm{St}, z/D) = E_4 \exp[-\mathrm{St}^{0{\cdot}75}] E_5 \exp\left[\frac{z/D - L/2D}{E_6}\right], \tag{18}$$

with

$$E_4 = 3{\cdot}0, \quad E_5 = 1{\cdot}9, \quad \text{and } E_6 = 1{\cdot}4.$$

The predictions based on equation (18) are shown compared to axial length-scales at $\theta_r = 140^\circ$ in Figure 11.

5. UNSTEADY FORCE PREDICTIONS

The unsteady lift and drag on the cylinder are calculated using equations (11) and (12) respectively, along with equations (13), (16) and (18). Two validations of the resultant model were performed. The first was a comparison of the r.m.s sectional unsteady lift and drag calculated with the model to sectional unsteady force measurements made on a cylinder with one free end (Baban *et al.* 1989). The Baban *et al.* results, normalized by dynamic head and sectional frontal area, for r.m.s. unsteady lift and drag at a section centered about $z/D = 1{\cdot}63$ were 0·37 and 0·71, respectively. The values of r.m.s. unsteady lift and drag predicted using the model were 0·33 and 0·65, respectively.

The second portion of the model validation was a comparison of the predicted results for the unsteady lift and drag spectra to unsteady force measurements performed on a cylindrical-shaped inertial hydrophone that was towed in deep water by McEachern & Lauchle (1995). The spectra are presented as a dimensionless fluctuating force spectrum, i.e. for the drag:

$$\left(\frac{G_{xx}(f)}{\rho U_\infty^2 A}\right)\left(\frac{U_\infty}{D}\right) \quad \text{versus} \quad \frac{fD}{U_\infty} \equiv \mathrm{St}. \tag{19}$$

Here, A (= LD) is the frontal area for the cylinder body.

Figure 12 shows the non dimensionalized lift and drag spectra predicted for the three Reynolds numbers considered. Note that the use of the reference autospectral density, $G_{p_r p_r}(f, \theta_r, z_r)$, in equation (11) results in a predicted unsteady force with a spectral character similar to that of the measured unsteady pressure data. The data are seen to collapse well using the inertial force and time scales of the flow for nondimensionalization. A comparison of the lift and drag spectra on the cylinder is shown in Figure 13 for Re = 19200. The predicted unsteady lift is typically 3 dB higher than the predicted unsteady drag over the entire range of Strouhal numbers. Measured sectional unsteady lift and drag coefficients on *infinite* cylinders are given by West & Apelt (1997). Their results show unsteady lift values that are 6–10 dB higher than the unsteady drag. In addition, their measured results on *finite- length* cylinders, showed that the sectional unsteady lift and drag coefficients are very similar in magnitude. The larger unsteady drag for the finite-length cylinder is attributed to the 3-D unsteady recirculation zone in the wake of the cylinder near the end-caps.

The spectral results presented by McEachern & Lauchle (1995) are for the combined unsteady lift and drag measured on a 2:1 aspect ratio cylindrical inertial hydrophone exposed to low Reynolds number cross-flow. A power summation (arithmetic addition) of the predicted lift and drag spectra enables a direct comparison to their results. The combined unsteady lift and drag spectrum predicted from the models, is denoted $G(f)$. Its comparison to the experimental results of McEachern & Lauchle (1995), is shown in

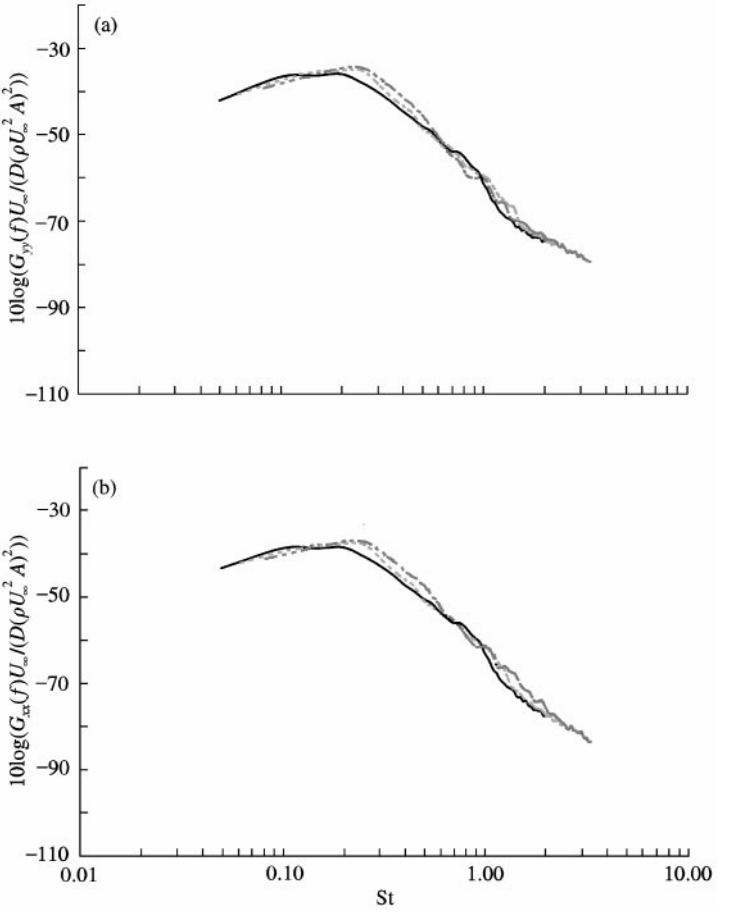

Figure 12. Unsteady lift and drag predictions for (a) unsteady lift and (b) unsteady drag: ——, Re = 32 000; – – –, Re = 25 600; – – – –, Re = 19 200.

Figure 14 for all three speeds. At high values of St, the model results agree to within 2 dB of the measured data.

6. CONCLUSIONS

The highest r.m.s. unsteady pressure levels were measured on the cylindrical surface near the end-caps, and in the rearward portion of the cylinder, aft of 110°. The high unsteady pressures near the end-cap are due to the 3-D separated flow over the cylinder ends. The high unsteady pressures in the rearward portion of the cylinder are due to the presence of a recirculation region behind the cylinder, and a local reattachment of the separated flow over the end-caps. Strong coherent vortex shedding from the cylinder is not present due to this end-induced disturbed flow region behind the cylinder that inhibits the vortex-formation process.

Near the mid-section of the cylinder, the Strouhal number dependence of the circumferential length-scales show a weak maximum near St = 0·21. The length-scales decrease as St^{-1} above this value. The decrease in length-scales with increasing Strouhal number is a result of the influence of small-scale, high-frequency, eddies. Below St = 0·21, the

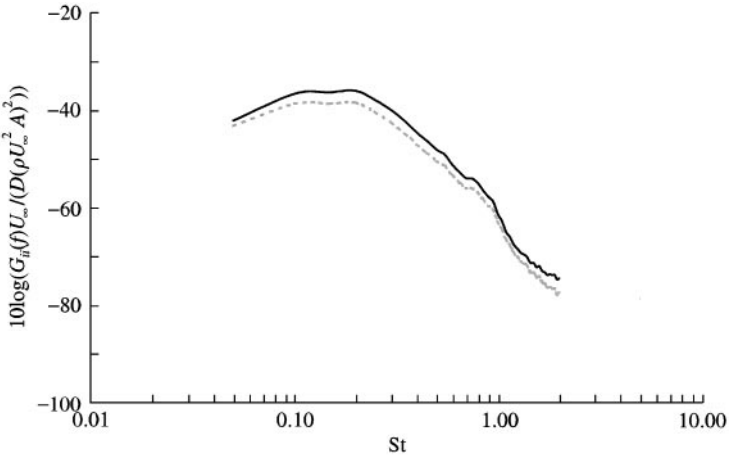

Figure 13. Unsteady lift versus unsteady drag predictions at Re = 19 200: ——, unsteady lift, $i = y$; – – –, unsteady drag, $i = x$.

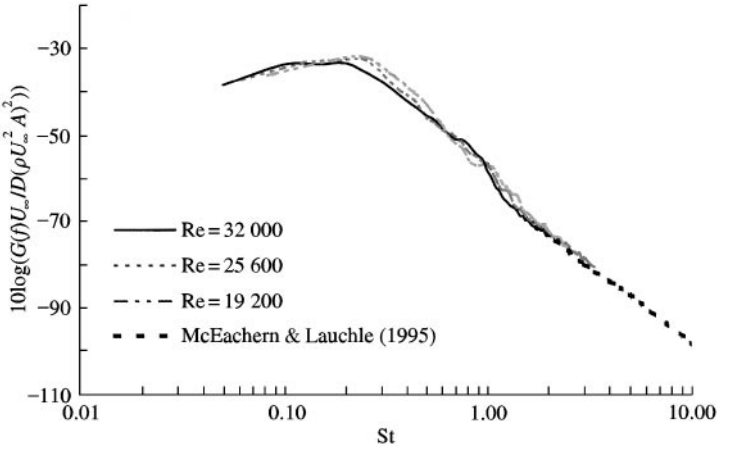

Figure 14. Predicted combination of unsteady lift and drag at Re = 32 000, 25 600, and 19 200 compared to the experimental data of McEachern & Lauchle (1995) over the range 4000 < Re < 18 000.

correlation lengths are also small (or nonexistent), due to the apparent inability of the flow to support large-scale structures. The circumferential length-scales, as a function of axial location, are relatively independent of z/D for $z/D > 0{\cdot}5$. For locations $z/D < 0{\cdot}5$, the length-scales are smaller and more sensitive to z/D due to the 3-D chaotic flow field near the end-cap.

The axial length-scales decrease exponentially with increasing Strouhal number. Due to the 3-D flow region near the end-caps, the axial length-scales depend on the reference location; the wall-pressure statistics are inhomogeneous. As the reference location is moved to the mid-sections of the cylinder, the axial length-scales approach values similar to those measured independently on 2-D cylinders.

The unsteady lift spectrum predicted for the cylinder is typically 3 dB higher than the predicted unsteady drag spectrum for the Reynolds numbers and cylinder aspect ratio considered in this study. This difference appears to be much less than it is for a 2-D cylinder which is more in the range of 10–12 dB. The increase in unsteady drag, and the decrease in

unsteady lift on the finite-length cylinder is apparently due to the incoherent recirculation zone created by cylinder end effects.

ACKNOWLEDGMENTS

The work reported here has been supported by ONR Code 321SS, Scott Littlefield, under grant number N00014-96-1-0005.

References

Baban, F., So, R. M. C. & Ottugen, M. V. 1989 Unsteady forces on circular cylinders in a cross-flow. *Experiments in Fluids* **7,** 293–302.

Bendat, J. S. & Piersol, A. G. 1986 *Random Data Analysis and Measurement Procedures*, 2nd edition. New York: John Wiley and Sons.

Corcos, G. M. 1964 The structure of the turbulent pressure field in boundary layer flows. *Journal of Fluid Mechanics*, **18,** 353–378.

Capone, D. E. 1999 Modeling the unsteady forces on a finite-length circular cylinder in cross-flow. Ph. D. thesis, The Pennsylvania State University, University Park, PA, U.S.A.

Crighton, D. C., Dowling, A. P., Ffowcs Williams, J. E., Heckl, M. & Leppington, F. G. 1994 *Modern Methods in Analytical Acoustics*, Lecture Notes, London: Springer-Verlag.

Farivar, D. J. 1981 Turbulent flow around cylinders of finite length. *AIAA Journal* **19,** 275–281.

Finger, R. A, Abbagnaro, L. A., & Bauer, B. B. 1979 Measurements of low-velocity flow noise on pressure gradient hydrophones. *Journal of the Acoustical Society of America*, **65**(6), 1407–1412.

Gershfeld, J. L. 1996 Sound generation from spatially inhomogeneous wall pressure fields. Ph.D. thesis, Catholic University of America, Washington, D. C., U.S.A.

Keefe, R. T. 1961 An investigation of the fluctuating forces acting on a stationary circular cylinder in a subsonic stream and of the associated sound field. Institute of Aerophysics, University of Toronto, UTIAS Report No. 76.

Lauchle, G. C. & Jones, A. R. 1998 Unsteady lift force on a towed sphere. *Journal of Fluids and Structures* **12,** 949–958

McEachern, J. F. 1993 The effect of body geometry on the flow noise of cylinders in cross flow. Ph. D. thesis, The Pennsylvania State University, University Park, PA, U.S.A.

McEachern, J. F. & Lauchle, G. C. 1995 Flow-induced noise on a bluff body. *Journal of the Acoustical Society of America* **97,** 947–953.

Ribeiro, J. L. D. 1992 Fluctuating lift and its spanwise correlation on a circular cylinder in a smooth and in a turbulent flow: a critical review. *Journal of Wind Engineering and Industrial Aerodynamics*, **40,** 179–198.

West, G. S. & Apelt, C. J. 1997 Fluctuating lift and drag on finite lengths of a circular cylinder in the subcritical Reynolds number range. *Journal of Fluids and Structures*, **11,** 135–158.